The second-order magnetic phase transition and magnetocaloric effect in all-d-metal NiCoMnTi-based Heusler alloys

Zhang, Fengqi; Westra, Kevin; Shen, Qi; Batashev, Ivan; Kiecana, Anika; van Dijk, Niels; Brück, Ekkes

DOI
10.1016/j.jallcom.2022.164337

Publication date
2022

Document Version
Final published version

Published in
Journal of Alloys and Compounds

Journal of Alloys and Compounds 906 (2022) 164337

Contents lists available at ScienceDirect

Journal of Alloys and Compounds

journal homepage: www.elsevier.com/locate/jalcom

Research Article

The second-order magnetic phase transition and magnetocaloric effect in all-*d*-metal NiCoMnTi-based Heusler alloys

Fengqi Zhang*, Kevin Westra, Qi Shen, Ivan Batashev, Anika Kiecana, Niels van Dijk, Ekkes Brück

Fundamental Aspects of Materials and Energy (FAME), Faculty of Applied Sciences, Delft University of Technology, Mekelweg 15, 2629JB Delft, The Netherlands

ARTICLE INFO

Article history:
Received 11 January 2022
Received in revised form 16 February 2022
Accepted 22 February 2022
Available online 24 February 2022

Keywords:
Magnetocaloric effect
All-*d*-metal
Ni(Co)MnTi
Heusler alloys
SOMT

ABSTRACT

The novel all-*d*-metal Ni(Co)MnTi based magnetic Heusler alloys provide an adjustable giant magnetocaloric effect and good mechanical properties. We report that the second-order magnetic phase transition can be tailored in this all-*d*-metal NiCoMnTi based Heusler system by optimizing the Mn/Ti ratio, resulting in a reversible ferromagnetic-to-paramagnetic magnetic transition. A candidate material $Ni_{33}Co_{17}Mn_{30}Ti_{20}$ with a magnetic entropy change ΔS_m of 2.3 $Jkg^{-1}K^{-1}$ for a magnetic field change of 0–5 T, has been identified. The T_C and saturation magnetization M_S can be controlled by adjusting the Ni/Co concentration and doping non-magnetic Cu atoms. The compositional maps of T_C and M_S have been established. Density functional theory (DFT) calculations reveal a direct correlation between the magnetic moments and the Co content. By combining XRD, SQUID, SEM and DFT calculations, the (micro)structural and magnetocaloric properties have been investigated systematically. This study provides a detailed insight in the magnetic phase transition for this all-*d*-metal Ni(Co)MnTi-based Heusler alloy system.

1. Introduction

The giant magnetocaloric effect (GMCE) is characterized by an adiabatic temperature change (ΔT_{ad}) and an isothermal magnetic entropy change (ΔS_m) when a magnetocaloric material (MCM) is exposed to a changing magnetic field. The GMCE can be utilized to design promising environmental-sustainable and eco-friendly applications like waste heat recovery, a thermomagnetic generator (TMG) and solid-state magnetic refrigeration (SSMR). The GMCE has been widely observed in various MCMs like Gd-Si-Ge [1], Fe_2P-type [2], La-Fe-Si [3], Ni-Mn-*X* (*X* = In, Sn, Sb, Ga, Al) based Heusler alloys [4] and Mn-*M*-X based (*M* = Co or Ni, X = Si or Ge) ferromagnets [5]. These materials demonstrate a strong first-order magnetic transition (FOMT) with a discontinuous change in the first derivative of the Gibbs free energy resulting from the coupling between the magnetic and crystal lattice degrees of freedom (in the form of a magnetoelastic or magnetostructural coupling). Even though the MCMs that show a FOMT exhibit the giant and sharp ΔS_m and ΔT_{ad}, the associated undesirable intrinsic thermal and magnetic hysteresis inevitably results in a low energy efficiency during cooling cycles as a result of the irreversibility. Furthermore, the strong crystal lattice distortion accompanied by the structural transition generally makes these MCMs subject to cracking and fatigue, which limits the lifetime of these materials.

Compared with the FOMT, the second-order magnetic transition (SOMT) with a discontinuous change in the second derivative of the Gibbs free energy show a reversible magnetic transition from the low-temperature ferromagnetic (FM) to high-temperature paramagnetic (PM) state. The SOMT materials can thereby avoid some of the intrinsic disadvantages of the FOMT materials, although the magnetocaloric performance is relatively moderate. Currently, some interesting SOMT materials like $(LaSr)MnO_3$ based perovskites [6], Fe-based amorphous alloys [7], $AlFe_2B_2$ based intermetallic compounds [8], MnSb based half-Heusler alloys [9,10] and NiMn based Heusler alloys [11–16] have been investigated. Singh *et al.* found that the off-stoichiometric $Ni_2Mn_{1.4}In_{0.6}$ Heusler alloys can simultaneously demonstrate a large saturation magnetization (M_S = 6.17 μ_B/f.u.) and a high ΔT_{ad} (of about 1.5 K for a field change of 0–2 T) near room temperature, which makes it competitive with some FOMT shape-memory Heusler alloys [11]. Additionally, the SOMT properties of the Si substituted $Ni_{50}Mn_{36}Sn_{14-x}Si_x$ (x = 1, 2, 3) and $Ni_{50}Mn_{35}In_{15-x}Si_x$ ($1 \le x \le 5$) Heusler systems have been studied [12,15]. Recently, the unique all-*d*-metal Ni(Co)MnTi based magnetic Heusler alloys have been discovered [17,18]. In comparison to the traditional NiMn-*X* (*X* = In, Sn, Sb, Ga, Al) based magnetic Heusler

* Corresponding author.
E-mail address: F.Zhang-7@tudelft.nl (F. Zhang).

https://doi.org/10.1016/j.jallcom.2022.164337
0925-8388/

alloys, where the 3rd element is mainly occupied by *p*-block elements, the structural transition temperature can be significantly decreased by introducing Ti and ferromagnetism can be established by forming strong Mn-Co-Mn magnetic interactions in these all-*d*-metal Ni(Co)MnTi based Heusler alloys. Like other Heusler systems, this all-*d*-metal Heusler alloy system also shows a large thermal hysteresis [19–21]. Because the Ti in the system can effectively stabilize the austenite phase [22], we therefore expect that tuning the Mn/Ti ratio could decouple the first-order magnetostructural transition, resulting in a reversible SOMT. Recent studies in this Heusler system mainly focus on regulating the FOMT [19,23]. Studies associated with the SOMT in this system are still scarce and could deepen our understanding of the functionality of this material system for future applications.

By optimizing the Mn/Ti ratio all-*d*-metal NiCoMnTi based magnetic Heusler alloys with a SOMT have been produced successfully. We systematically investigate the magnetocaloric properties (including compositional maps of T_C and M_S), the structural properties and the microstructure information of these alloys by XRD, SQUID, SEM and Density functional theory (DFT). Our results show T_C and M_S can be controlled by adjusting the Ni/Co concentration and by doping non-magnetic Cu atoms. The present study provides new insight into the magnetic phase transition for this all-*d*-metal Ni(Co)MnTi based Heusler alloy system.

2. Experimental methods

The SOMT all-*d*-metal NiCoMnTi based magnetic Heusler alloys with a composition of $Ni_{50-x}Co_xMn_{30}Ti_{20}$ (x = 11, 12, 13, 15, 17, 19, 21, 23), $Ni_{37}Co_{13}Mn_{30+x}Ti_{20-x}$ (x = 1, 2), $Ni_{33}Co_{17}Mn_{30-x}Ti_{20+x}$ (x = 2, 4) and $Ni_{37-y}Co_{13}Mn_{30}Ti_{20-x}Cu_{x+y}$ (x,y = 0.5, 1) samples were prepared from high-purity elements (Ni 99.99%, Co 99.9%, Mn 99.99%, Ti 99.99% and Cu 99.9%) through the arc-melting technique under Ar atmosphere. For homogenization the melted ingots were flipped and remelted for five times. An extra 4% Mn was added to compensate for evaporation losses during melting. Subsequently, the as-cast ingots were sealed into quartz ampoules under Ar atmosphere and annealed at 1173 K for 6 days followed by cold-water quenching to further enhance homogeneity and short range order. The room temperature X-ray diffraction (XRD) patterns were collected on a PANalytical X-pert Pro diffractometer with Cu-K_α radiation. The crystal structure refinement of XRD patterns was performed using the Rietveld refinement method [24] implemented in the Fullprof software package. The microstructure of the alloys was analyzed by a Scanning Electron Microscope (SEM, JEOL JSM IT100LA) equipped with Energy Dispersive X-ray Spectroscopy (EDS), and line-scans were used to determine the elemental distribution of different phases. To visualize the grain boundaries of the materials two drops of etching solvent (0.5 g $FeCl_3$ mixed with 9.9 mL methanol (CH_3OH)) were spread on the surface of metallographic specimens and then rapidly removed with ethanol after 15–20 s. After that, optical microscopy (Olympus Corporation) was applied. The temperature and magnetic field dependence of the magnetization curves were characterized by a superconducting quantum interference device (SQUID) magnetometer (Quantum Design MPMS 5XL) using the reciprocating sample option (RSO) mode. For measurements on the magnetic properties above 370 K a vibrating sample magnetometer (VSM, Quantum Design Versalab) was applied. The ΔS_m and ΔT_{ad} can be derived from the calorimetric measurements based on a home-built in-field DSC machine, details can be found in Ref. [25].

First-principles electronic structure calculations were performed in the framework of the density functional theory (DFT). The Vienna ab initio simulation package (VASP) [26,27] in the projector augmented wave (PAW) method [28,29] was employed to perform the DFT calculations using the generalized gradient approximation of Perdew-Burke-Ernzerhof [30] for the exchange correlation functional. The valence electron configuration was $3p^64s^23d^5$ for Mn, $3p^64\ s^23d^2$ for Ti, $4s^23d^7$ for Co and $4s^23d^8$ for Ni. A 2 × 2 × 1 supercell, built from a 16-atom unit cell, was utilized in all calculations. The structural degrees of freedom were fully relaxed on a *k*-grid of 10 × 10 × 10. The *k*-space integrations were performed with the Methfessel-Paxton method [31] of second order with a smearing width of 0.05 eV. The lattice parameters and atomic positions were relaxed for a force convergence of 0.1 meV/Å, the energies were converged to 1 μeV. The kinetic energy cutoff was set at 350 eV.

3. Results and discussion

3.1. Structural analysis

The room temperature XRD patterns for the $Ni_{50-x}Co_xMn_{30}Ti_{20}$ (x = 12, 13, 15, 17, 19, 21, 23) samples are shown in Fig. 1(a). All diffraction peaks correspond with the cubic B_2-type austenite (space group *Fm-3 m*) crystal structure, confirming that a stable austenite phase is formed. No signal from the modulated martensite structure or from an impurity phase was found, indicating a pure austenite phase. Wei *et al.* demonstrated that samples contained less than 16% Co could hold martensite at low temperatures [17], while in our case the martensite to austenite structural transition can be tuned to disappear and only the parent B_2-type austenite is left by optimizing Mn/Ti ratio to a lower Mn level (higher Ti). The lattice parameter *a* decreases from 5.928 Å to 5.914 Å when the Co content increases from 12% to 23%, as illustrated in Fig. 1(b). Considering the covalent radius of Ni (1.24 Å) and Co (1.26 Å) [32], more Co with a larger radius should expand the unit-cell volume, which is in conflict with the experimental results. Similar results were also observed in $Ni_{50-x}Co_xMn_{35}Ti_{15}$ (x = 13, 13.5) ribbon samples with a FOMT [20]. This decrease in cell volume is also confirmed by our DFT calculations see below. The Rietveld refinement of the room-temperature XRD pattern for the $Ni_{33}Co_{17}Mn_{30}Ti_{20}$ sample is presented in Fig. 1(c) and the main diffraction planes are labeled as (220), (400) and (422). In Fig. 1(d) the cubic B_2 austenite crystal structure with space group *Fm-3 m* is shown. The various metallic atoms follow specific crystal occupancy rules. The Ni/Co atoms occupy the *8c* site at (1/4, 1/4, 1/4) and (1/4, 1/4, 3/4) while the Mn/Ti atoms occupy the *4b* site at (1/2, 1/2,1/2) and the *4a* site at (0, 0, 0), where Mn preferentially occupies the *4b* position.

3.2. Magnetic properties and magnetic phase diagram

In Fig. 2(a) the temperature-dependent magnetization (*M-T*) curves of the materials that vary in Ni/Co ratio (x = 12, 13, 15, 17, 19, 21, 23) are shown. The heating and cooling curves coincide, which suggests that the transition corresponds to a SOMT. The results show that the magnetic behavior is significantly affected by its composition. For instance, a higher Co content attributes to an obvious enhancement in magnetization. By comparing the samples with the lowest Co (12%) and the highest Co (23%) it is found that the saturation magnetization shows a fivefold increment, from 32.4 to 144.5 Am^2kg^{-1}. Similar to the case of all-*d* metal NiCoMnTi system with a FOMT, the so-called "Co-activated ferromagnetism" also plays a crucial function in the SOMT system where Co can effectively help to build a strong ferromagnetic coupling in the local Mn-Co-Mn configuration [33,34]. In Fig. 2(b), the *M-T* curves at 0.01 T are presented. The Curie temperature T_C of austenite can be determined from the maximum in $|dM/dT|$ in these low-field *M-T* curves (see the inset of Fig. 2(b)). As illustrated in Fig. 2(c), it can be seen that with increasing Co content the T_C of austenite increases and closely follows a linear relation of about 27 K/at% Co. Interestingly, in Fig. 2(b) we observe for almost all samples a distinct difference between zero-field-cooling (ZFC) and field-cooling (FC) curves when temperature is below 100 K. This has also been observed in other Mn-

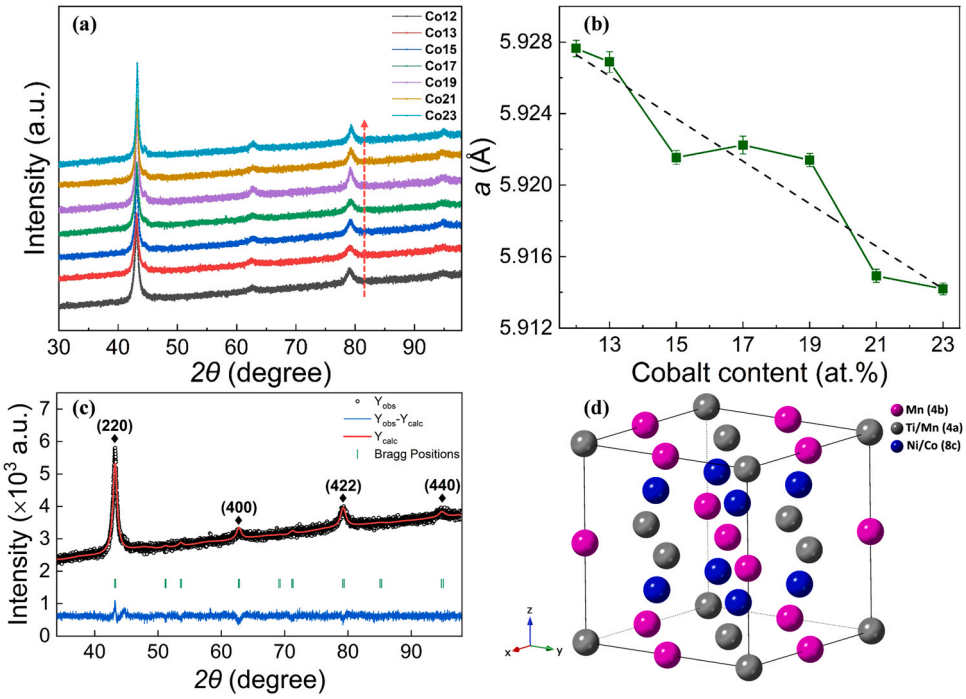

Fig. 1. (a) Room-temperature XRD patterns for $Ni_{50-x}Co_xMn_{30}Ti_{20}$ (x = 12, 13, 15, 17, 19, 21, 23) alloys with different Co concentrations. (b) Lattice parameter a derived from the XRD refinement results as a function of the Co concentration for the $Ni_{50-x}Co_xMn_{30}Ti_{20}$ (x = 12, 13, 15, 17, 19, 21, 23) alloys. (c) Room-temperature refined XRD measurement of the $Ni_{33}Co_{17}Mn_{30}Ti_{20}$ sample. (d) Schematic crystal structures of B_2 austenite phase.

based Heusler alloys like Fe-Mn-Si [35] and Ni-Mn-In [13] and should be ascribed to magnetocrystalline anisotropy. The maximum observed in the temperature dependence of the magnetization for Co ≤ 19 should be ascribed to a change in magnetic interactions from FM at high temperatures to antiferromagnetic (AFM) at lower temperature. Note, that the parent austenite of NiMnTi based Heusler alloys is an antiferromagnet [17,19]. In Fig. 2(d) the isothermal field-dependent magnetization (M-H) curves at 5 K are presented, which demonstrate that an increase in Co concentration leads to a higher magnetization. Furthermore, it can be also deduced that considerably less magnetic field is needed to reach its maximum magnetization for samples with a higher Co content. For example, the sample containing 23% Co can be saturated at around 1 T while the 15% Co sample is still not saturated at 5 T. It is worth to note that for the samples with the lowest Co content (such as 12% and 15%) the magnetization and demagnetization curves fail to overlap each other below 1 T, which should also be attributed to the magnetocrystalline anisotropy mentioned above.

Controlling T_C to cover a certain temperature range is a fundamental requirement for cooling applications. The Curie temperature can be tuned via optimizing different intrinsic and extrinsic parameters, such as composition [36], particle size [37], chemical element pressure [38], electron valence [23], and external mechanical (hydrostatic) pressure [39]. Within these factors, the chemical pressure, which is closely related to a change in unit-cell volume, and electron valence effects could be distinctly affected by magnetic/non-magnetic metal substitution or interstitial (light-element) doping. For example, the substitution of Mn by Cr has been applied to tailor the magnetic and structural transitions in $Mn_{1-x}Cr_xCoGe$ compounds [40]. Recently, it has been found that Cu substitution in Ni-Mn-In based Heusler alloys can effectively modify the FOMT [41–43]. Therefore, we expect that T_C could also be efficiently tailored through Cu substitution of Ni/Mn in the Ni-Co-Mn-Ti system with a SOMT. In Fig. 3(a), the M-T curves at 1 T for the $Ni_{37-y}Co_{13}Mn_{30}Ti_{20-x}Cu_{x+y}$ (x,y = 0, 0.5, 1) samples are presented. It is observed that the magnetization decreases when Cu replaces Ti or Ni. In Fig. 3(b) it is shown that compared with the parent $Ni_{37}Co_{13}Mn_{30}Ti_{20}$ (T_C = 202 K) alloy, Cu substitution of Ti shows a remarkable decrease in T_C. A substitution of 0.5% Cu shifted T_C to 179 K (and 1% Cu to 171 K), while a 0.5% Cu substitution of Ni results in a reduction in T_C to 190 K (and 1% Cu to 178 K). The reduction in T_C is about 24 K/at% Cu. The shift in T_C by Cu substitution could result from the weakened magnetic exchange interaction between the Mn-Co-Mn configuration, rather than the chemical pressure effect because the covalent radius of Cu (1.32 Å) is in between that of Ti (1.60 Å) and Ni (1.24 Å) [32], even though Cu ($3d^{10}4s^1$) atoms have more electrons than Ti ($3d^24s^2$)/Ni ($3d^84s^2$). Therefore, Cu substitution and tuning the Ni/Co ratio are both efficient ways to optimize the T_C shift. In addition, Fig. 3(c) and 3(d) show the M-T curves at 1 T for the $Ni_{37}Co_{13}Mn_{30+x}Ti_{20-x}$ (x = 0, 1, 2) and $Ni_{33}Co_{17}Mn_{30-x}Ti_{20+x}$ (x = 0, 2, 4) samples.

From the above results it can be seen that T_C and the magnetization can be regulated by composition in the $Ni_{50-x}Co_xMn_{30}Ti_{20}$ (x = 12, 13, 15, 17, 19, 21, 23) samples with a SOMT. This indicates that Co substitution for Ni is effective in increasing T_C and the magnetization for the NiCoMnTi Heusler alloys with a SOMT. This may be attributed to the strong coupling between Co and Mn atoms. A similar phenomenon was also observed in other NiMn-based Heusler alloys with a FOMT, such as Ni(Co)MnGa [44], Ni(Co)MnIn [45], Ni(Co)MnSn [46] and Ni(Co)MnSb [47]. In Fig. 4(a) and 4(b) we summarized the changes in T_C and magnetization as a function of Co content. Once Co content is above 12 at% T_C and magnetization data show an increasing tendency with increasing Co concentration, and T_C of 11% Co is close to 12% one.

To better guide the optimization of the all-d-metal NiCoMnTi magnetic Heusler alloys with a SOMT, it is useful to determine compositional maps of the saturation magnetization M_S and the Curie temperature T_C with respect to different Co/Ti content (in at %), as presented in Fig. 4(c) and 4(d), respectively. On the other hand, to verify the usefulness of these phase diagrams, two new alloys with a designed composition ($Ni_{29}Co_{21}Mn_{28}Ti_{22}$ and $Ni_{28}Co_{22}Mn_{26}Ti_{24}$) are utilized. For example, Fig. 5 shows the M-T

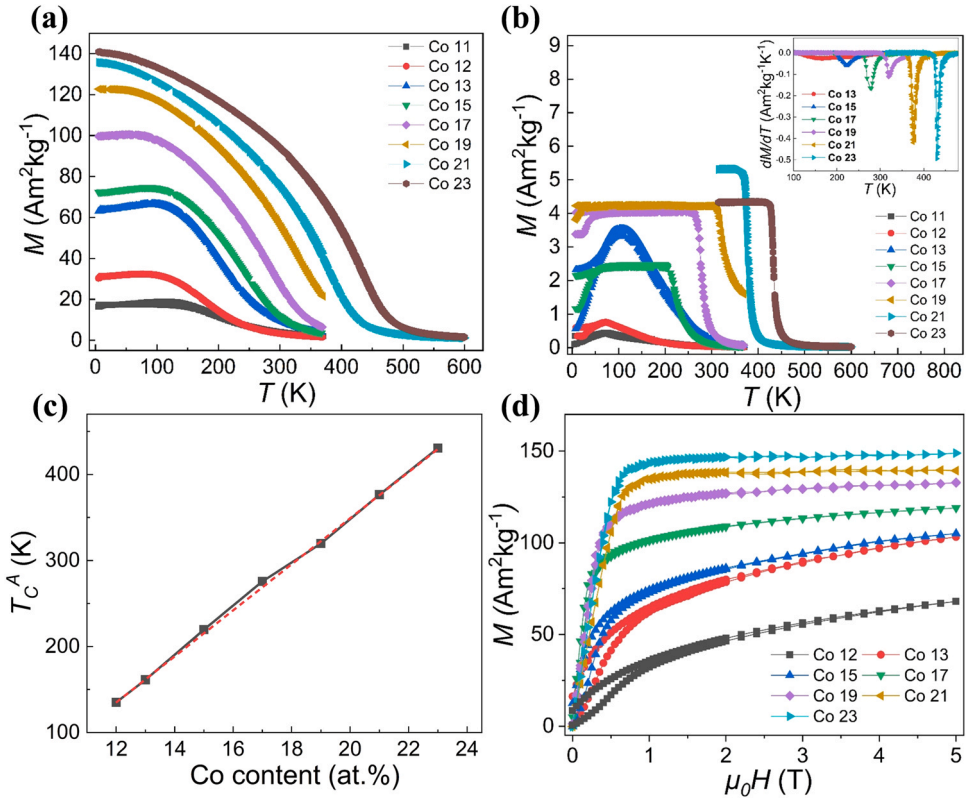

Fig. 2. (a) Temperature-dependent magnetization (*M-T*) curves at 1 T for $Ni_{50-x}Co_xMn_{30}Ti_{20}$ (x = 12, 13, 15, 17, 19, 21, 23) samples. (b) *M-T* curves at 0.01 T for $Ni_{50-x}Co_xMn_{30}Ti_{20}$ (x = 12, 13, 15, 17, 19, 21, 23) samples. The inset shows *dM/dT* versus temperature. (c) Curie temperature as a function of the Co content. (d) Field-dependent magnetization (*M-H*) curves at 5 K for $Ni_{50-x}Co_xMn_{30}Ti_{20}$ (x = 12, 13, 15, 17, 19, 21, 23) samples.

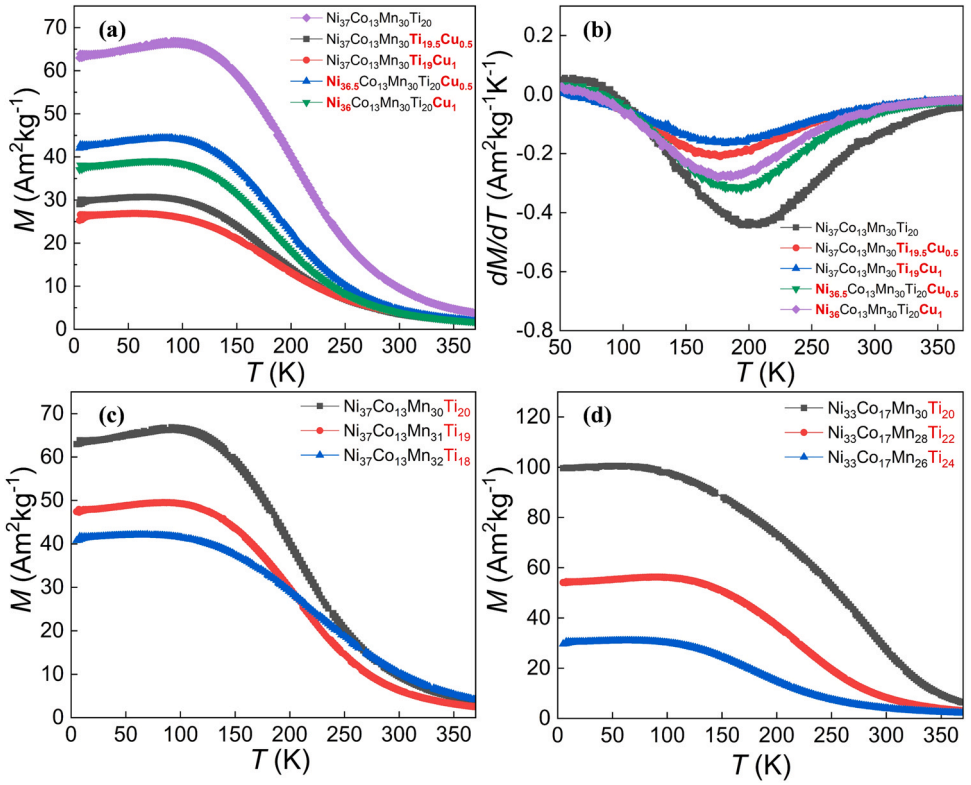

Fig. 3. (a) Isofield *M-T* curves at 1 T for $Ni_{37-y}Co_{13}Mn_{30}Ti_{20-x}Cu_{x+y}$ (x,y = 0, 0.5, 1) series samples. (b) Relationship between *dM/dT* and temperature for the Cu-doped samples. (c) Isofield *M-T* curves at 1 T for $Ni_{37}Co_{13}Mn_{30+x}Ti_{20-x}$ (x = 0, 1, 2) samples. (d) Isofield *M-T* curves at 1 T for $Ni_{33}Co_{17}Mn_{30-x}Ti_{20+x}$ (x = 0, 2, 4) samples.

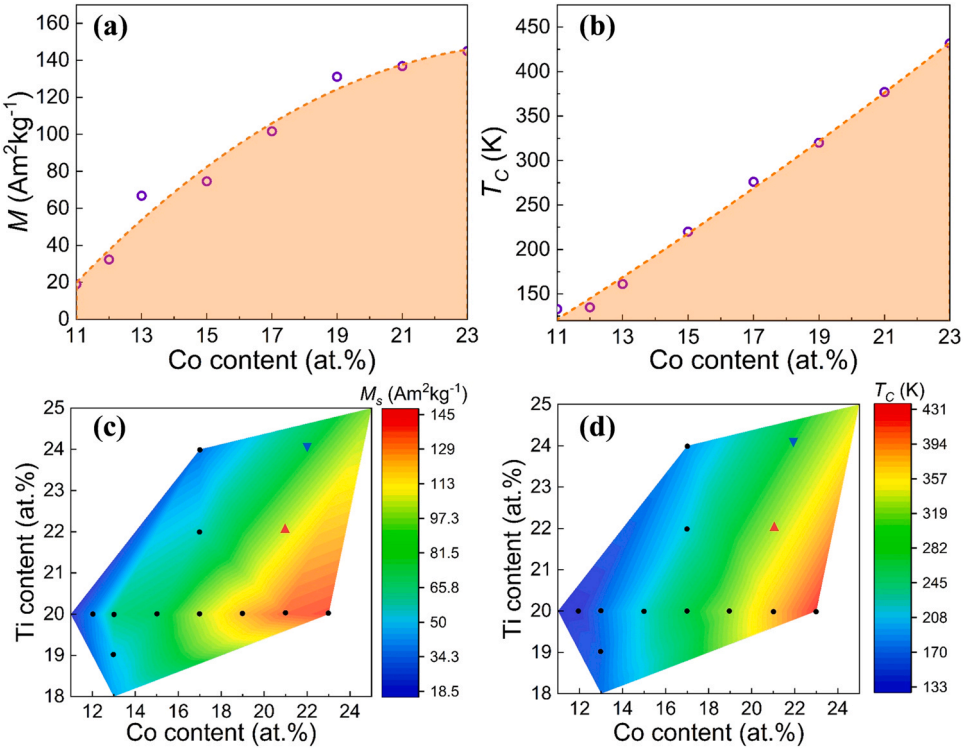

Fig. 4. Effect of the Co concentration on the (a) saturation magnetization and (b) transition temperature at 5 K derived from *M-T* measurements. Effect of the amount of Co and Ti substitution on (c) the saturation magnetization and (d) the phase transition temperature the 2D compositional maps. The black marks indicate which compositions were measured, and (▲?), (▼?) in the top corner stands for two test samples to confirm the trends.

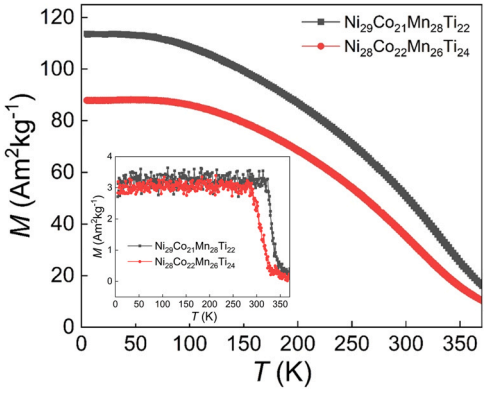

Fig. 5. Isofield *M-T* curves at 1 T for the $Ni_{29}Co_{21}Mn_{28}Ti_{22}$ and $Ni_{28}Co_{22}Mn_{26}Ti_{24}$ samples. The inset corresponds to the *M-T* curves at 0.01 T for these two alloys.

curves at 1 T for these two samples and the inset corresponds to the *M-T* curves at 0.01 T. The values of M_S at 5 K are 114 and 88 Am^2kg^{-1}, and the values of T_C are 333 and 311 K for $Ni_{29}Co_{21}Mn_{28}Ti_{22}$ and $Ni_{28}Co_{22}Mn_{26}Ti_{24}$ compounds, respectively. These experimental data points are marked in Fig. 4(c) and 4(d). It is clear that the experimental data for these two samples are in good agreement with the compositional maps for T_C and M_S, which supports the reliability of our compositional maps.

Using DFT, the calculated lattice parameter *a*, the total magnetic moment and the lowest formation energy have been evaluated for the $Ni_{50-x}Co_xMn_{30}Ti_{20}$ (x = 12, 13, 15, 17, 19, 21, 23) samples, as listed in Table 1. A decrease in lattice parameter *a* is also observed for increasing Co content, which is in agreement with our experimental results shown in Fig. 1(b). Interestingly, the total magnetic moment (per formula unit) for this material system with a SOMT is predominantly controlled by the Co concentration and shows an increase with increasing Co content. For instance, the calculated moment was enhanced from 5.44 (x = 13) to 5.83 (x = 23) μ_B/f.u. This might be because a higher Co content can more sufficiently align the Mn atoms as the local Mn-Co-Mn configuration controls the introduced strong FM, which is similar to other Co-doping NiMn-based Heusler systems.

Table 1
DFT calculation results for the lattice parameters *a*, the total magnetic moment per formula unit and the lowest formation energy for the $Ni_{50-x}Co_xMn_{30}Ti_{20}$ (x = 12, 13, 15, 17, 19, 21, 23) samples.

x	13	14	16	17	19	20	22	23
a (Å)	5.91	5.91	5.90	5.89	5.88	5.88	5.87	5.87
Moment (μ_B/f.u)	5.44	5.45	5.55	5.60	5.64	5.71	5.80	5.83
Energy (*eV*/atom)	-0.668	-0.641	-0.631	-0.612	-0.591	-0.575	-0.544	-0.517

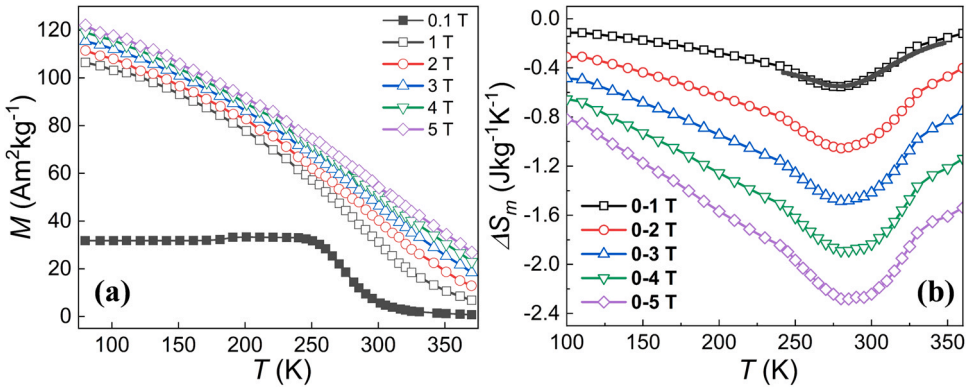

Fig. 6. (a) Isofield *M-T* curves between 0.1 and 5 T for the $Ni_{33}Co_{17}Mn_{30}Ti_{20}$ sample. (b) Magnetic entropy change ΔS_m for different magnetic field changes as a function of temperature for the $Ni_{33}Co_{17}Mn_{30}Ti_{20}$ sample. The black solid curve was derived from DSC-in field measurement with $\Delta\mu_0 H$ = 1 T.

Due to the relative high M_S at 1 T (102 Am^2kg^{-1}) and the near room temperature magnetic phase transition T_C (275 K) the 17% Co sample ($Ni_{33}Co_{17}Mn_{30}Ti_{20}$) seems to be the most promising candidate within this series for magnetic refrigeration applications. It is therefore of interest to further investigate the magnetocaloric properties of this $Ni_{33}Co_{17}Mn_{30}Ti_{20}$ alloy in terms of the magnetic entropy change (ΔS_m), adiabatic temperature change (ΔT_{ad}) and the relative cooling power (*CRP*). As shown in Fig. 6(a), the isofield *M-T* curves from 0.1 to 5 T have been collected. From these data the ΔS_m values can be calculated by using the Maxwell relation:

$$\Delta S_m(T, \quad H) = \int_0^{\mu_0 H} \left(\frac{\partial M}{\partial T}\right)_H d\mu_0 H \tag{1}$$

From Fig. 6(b) it can be seen that the sample shows a conventional MCE. As expected for a material with a SOMT the ΔS_m peak is obviously broad and moderate in size. For example, the maximum $|\Delta S_m|$ with an applied magnetic field change ($\Delta\mu_0 H$) of 0–1 T can reach only 0.6 $Jkg^{-1}K^{-1}$ which is well consistent with the value extracted from DSC-in field measurement, and $|\Delta S_m|$ reaches a maximum value of 1.1 and 2.3 $Jkg^{-1}K^{-1}$ with $\Delta\mu_0 H$ of 0–2 and 0–5 T, respectively. Although maximum value for $|\Delta S_m|$ only reaches about 22% of the value obtained for pure gadolinium (5 $Jkg^{-1}K^{-1}$ for $\Delta\mu_0 H$ = 2 T), it is comparable to other magnetic Heusler alloys with a SOMT [11–14,48,49]. The coefficient of refrigerant performance (*CRP*) reflects the MCE performance and can be determined by the following relation [50]:

$$CRP = \frac{\Delta S_m^{max} \Delta T_{ad}}{\int_0^{\mu_0 H} M(Tc, H) d\mu_0 H} \tag{2}$$

where $|\Delta S_m^{max}|$ is maximum peak value of $|\Delta S_m|$ and ΔT_{ad} is the maximum temperature change (extracted from in-field DSC measurements) due to an applied magnetic field ($\Delta T_{ad} \approx 0.3$ K for $\Delta\mu_0 H$ = 1 T). Therefore, compared with commercial Gd (≈ 0.17(2) for $\Delta\mu_0 H$ = 1 T) the calculated *CRP* value for $Ni_{33}Co_{17}Mn_{30}Ti_{20}$ alloy is only 0.01 which means this material is not suitable for potential magnetic refrigeration application.

3.3. Microstructural information

If the crystal structure and the macroscopic property change, then it is useful to obtain a deeper insight into the microstructure. For some traditional NiMn-*X* (*X* = In, Sn, Sb, Ga, Al) based magnetic Heusler alloys, the average grain size can reach several hundreds of μm up to the mm-range [23]. As demonstrated in Fig. 7(a), the grain boundaries of the material are distinguishable in the optical microscopy image, and the average grain size is approximately 100–200 μm. Compared with other NiMn-*X* (*X* = In, Sn, Sb, Ga, Al) based Heusler alloys, this grain size is significantly smaller. Considering the Hall-Petch relation (inverse relation between the grain size and the material strength) [51] the noticeable reduction in grain size for the NiCoMnTi MCMs with a SOMT could lead to an enhanced mechanical strength. Grain refinement has been utilized in NiCoMnTi ribbon samples with a FOMT to improve micro-hardness [20]. Additionally, as shown in the SEM image of Fig. 7(b), pure austenite is observed and there is no slat-like martensite at room temperature. Worth mentioning is the presence of several μm (below 10 μm) secondary phase precipitates within the main matrix. Because the concentration of precipitates is very limited (< 1%), it is insufficient to be detected by XRD. EDS measurements were utilized to determine the composition of main matrix phase and the secondary phase, as illustrated in Table 2. The chemical composition of the main matrix phase ($Ni_{32.57}Co_{16.33}Mn_{31.87}Ti_{19.06}$) is close to the nominal composition ($Ni_{33}Co_{17}Mn_{30}Ti_{20}$). Meanwhile, the small fraction of precipitates corresponds to a Ti-rich impurity ($Ni_{2.69}Co_{1.33}Mn_{4.76}Ti_{91.22}$). The concentration of Ti-rich second phase particles can be controlled by the annealing conditions. For instance, a lower heat-treatment temperature would generate more Ti-rich impurities. The enlarged SEM image in Fig. 7(c) shows the morphology of the Ti-rich secondary phase. In the SEM figure of Fig. 7(c) a line scan measurement was performed at various locations along the yellow dashed line to confirm the elemental distribution of the main matrix phase and the Ti-rich secondary phase, as shown in Fig. 7(d). The line scans indicate that the Ti-rich impurities are quite homogeneous.

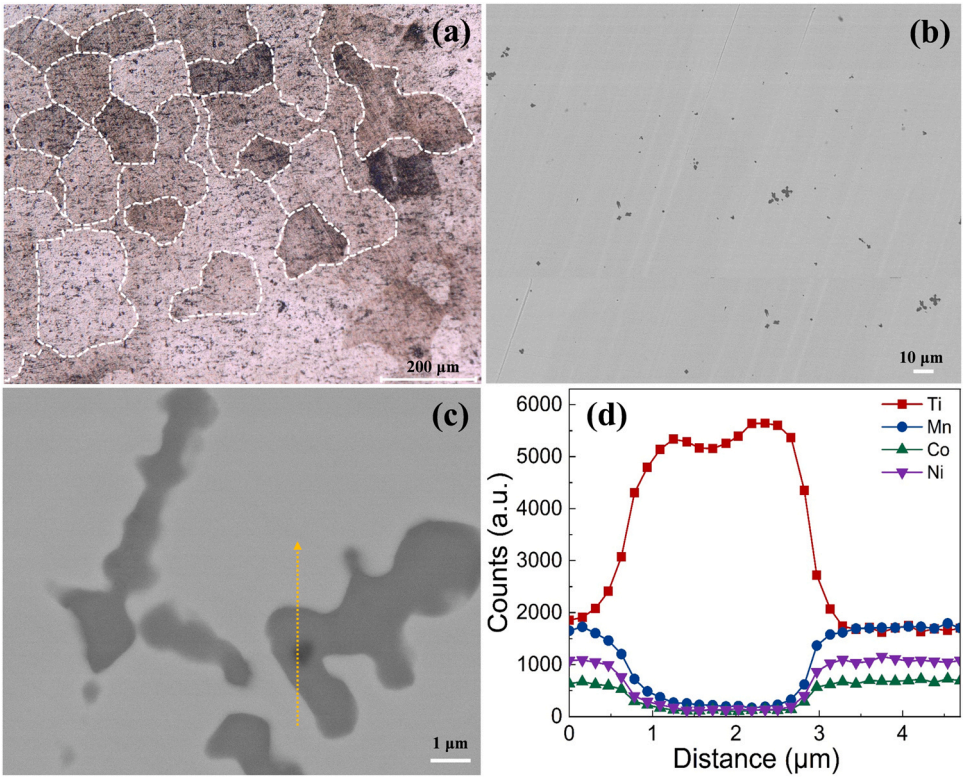

Fig. 7. (a) Optical microscope image for the etched $Ni_{33}Co_{17}Mn_{30}Ti_{20}$ sample. (b) Back-scattered SEM image for the $Ni_{33}Co_{17}Mn_{30}Ti_{20}$ sample. (c) Enlarged back-scattered SEM image for the $Ni_{33}Co_{17}Mn_{30}Ti_{20}$ sample. (d) SEM line scan measurements based on (c) for the $Ni_{33}Co_{17}Mn_{30}Ti_{20}$ sample.

Table 2
Elemental composition of the $Ni_{33}Co_{17}Mn_{30}Ti_{20}$ alloy determined by EDS measurements.

	Ni (*at%*)	Co (*at%*)	Mn (*at%*)	Ti (*at%*)
Main phase	32.57 (± 0.99)	16.33 (± 0.87)	31.87 (± 0.88)	19.06 (± 0.47)
Ti-rich impurity	2.69 (± 0.61)	1.33 (± 0.44)	4.76 (± 0.44)	91.22 (± 1.00)

4. Conclusions

In summary, by utilizing XRD, SQUID, SEM measurements and DFT calculations the crystal structural, the magnetocaloric properties and the microstructure information have been investigated systematically in the novel all-*d*-metal NiCoMnTi based magnetic Heusler alloys with a SOMT. The Mn/Ti ratio controls the FOMT/SOMT nature of transition. The SOMT in this alloy system is obtained by optimizing the Mn/Ti ratio. The values of T_C and M_S can be regulated by adjusting either by the Ni/Co ratio or by doping with non-magnetic Cu. The alloys with a high Co content show good soft magnetic properties with a reversible ferromagnetic transition and a moderate MCE. Compositional maps for T_C and M_S have been established. The microstructural measurements indicate that the refined crystallite size and limited volume fraction of the Ti-rich secondary phase. The DFT calculations reveal that the total magnetic moment per formula unit is controlled by the Co content. Our study provides new insight on the second-order magnetic phase transition for these all-*d*-metal Ni(Co)MnTi based Heusler alloys.

CRediT authorship contribution statement

Fengqi Zhang: Investigation, Methodology & writing; **Kevin Westra:** Investigation & writing; **Qi Shen:** Microstructural Investigation; **Ivan Batashev:** DFT calculation; **Anika Kiecana:** Microstructural Investigation; **Niels van Dijk:** Supervision, Writing – review & editing; **Ekkes Brück:** Supervision, Writing – review & editing.

Declaration of Competing Interest

The authors declare that they have no known competing financial interests or personal relationships that could have appeared to influence the work reported in this paper.

Acknowledgements

The authors thank Anton Lefering, Bert Zwart, Robert Dankelman and Michel Steenvoorden for their technical assistance. This work was sponsored by NWO in the domain of the Applied and Engineering Sciences (AES) program. Fengqi Zhang gratefully acknowledges financial support from the China Scholarship Council.

References

[1] V.K. Pecharsky, K.A. Gschneidner, Giant magnetocaloric effect in $Gd_5(Si_2Ge_2)$, Phys. Rev. Lett. 78 (1997) 4494–4497.
[2] O. Tegus, E. Brück, K.H.J. Buschow, F.R. de Boer, Transition-metal-based magnetic refrigerants for room-temperature applications, Nature 415 (2002) 150–152.
[3] F.X. Hu, B.G. Shen, J.R. Sun, Z.H. Cheng, G.H. Rao, X.X. Zhang, Influence of negative lattice expansion and metamagnetic transition on magnetic entropy change in the compound $LaFe_{11.4}Si_{1.6}$, Appl. Phys. Lett. 78 (2001) 3675–3677.
[4] A. Planes, L. Mañosa, M. Acet, Magnetocaloric effect and its relation to shape-memory properties in ferromagnetic Heusler alloys, J. Phys. Condens. Mater. 21 (2009) 233201.
[5] J. Liu, Y.Y. Gong, Y.R. You, X.M. You, B.W. Huang, X.F. Miao, G.Z. Xu, F. Xu, E. Brück, Giant reversible magnetocaloric effect in MnNiGe-based materials: Minimizing thermal hysteresis via crystallographic compatibility modulation, Acta Mater. 174 (2019) 450–458.

[6] J. Mira, J. Rivas, F. Rivadulla, C. Vazquez-Vazquez, M.A. Lopez-Quintela, Change from first- to second-order magnetic phase transition in $La_{2/3}(Ca,Sr)_{1/3}MnO_3$ perovskites, Phys. Rev. B 60 (1999) 2998–3001.

[7] X.C. Zhong, H.C. Tian, S.S. Wang, Z.W. Liu, Z.G. Zheng, D.C. Zeng, Thermal, magnetic and magnetocaloric properties of $Fe_{80-x}M_xB_{10}Zr_9Cu_1$ (M = Ni, Ta; x=0, 3, 5) amorphous alloys, J. Alloy. Compd. 633 (2015) 188–193.

[8] X.Y. Tan, P. Chai, C.M. Thompson, M. Shatruk, Magnetocaloric effect in $AlFe_2B_2$: toward magnetic refrigerants from earth-abundant elements, J. Am. Chem. Soc. 135 (2013) 9553–9557.

[9] E.E. Levin, J.D. Bocarsly, K.E. Wyckoff, T.M. Pollock, R. Seshadri, Tuning the magnetocaloric response in half-Heusler/Heusler $MnNi_{1+x}Sb$ solid solutions, Phys. Rev. Mater. 1 (2017) 075003.

[10] J.A. Cooley, M.K. Horton, E.E. Levin, S.H. Lapidus, K.A. Persson, R. Seshadri, From waste-heat recovery to refrigeration: compositional tuning of magnetocaloric $Mn_{1+x}Sb$, Chem. Mater. 32 (2020) 1243–1249.

[11] S. Singh, L. Caron, S.W. D'Souza, T. Fichtner, G. Porcari, S. Fabbrici, C. Shekhar, S. Chadov, M. Solzi, C. Felser, Large magnetization and reversible magnetocaloric effect at the second-order magnetic transition in Heusler materials, Adv. Mater. 28 (2016) 3321–3325.

[12] G.R. Raji, A.P. Paulose, R.B. Job, S. Thomas, K.G. Suresh, M.R. Varma, Phase transformations, inverse magnetocaloric effect and critical behavior of $Ni_{50}Mn_{36}Sn_{14-x}Si_x$ Heusler alloys, Intermetallics 82 (2017) 59–67.

[13] B. Dahal, C. Huber, W.Y. Zhang, S. Valloppilly, Y. Huh, P. Kharel, D. Sellmyer, Effect of partial substitution of In with Mn on the structural, magnetic, and magnetocaloric properties of $Ni_2Mn_{1+x}In_{1-x}$ Heusler alloys, J. Phys. D Appl. Phys. 52 (2019) 1–8.

[14] B.R. Dahal, Z. Lehmann, Y. Huh, P. Kharel, Magnetocaloric effect in $Ni_2Mn_xFe_yIn_z$ Heusler alloys with second-order phase transition, AIP Adv. 10 (2020) 015109.

[15] A.K. Pathak, I. Dubenko, S. Stadler, N. Ali, The effect of partial substitution of In by Si on the phase transitions and respective magnetic entropy changes of $Ni_{50}Mn_{35}In_{15}$ Heusler alloy, J. Phys. D Appl. Phys. 41 (2008) 202004.

[16] I. Dubenko, M. Khan, A.K. Pathak, B.R. Gautam, S. Stadler, N. Ali, Magnetocaloric effects in Ni-Mn-X based Heusler alloys with X = Ga, Sb, In, J. Magn. Magn. Mater. 321 (2009) 754–757.

[17] Z.Y. Wei, E.K. Liu, J.H. Chen, Y. Li, G.D. Liu, H.Z. Luo, X.K. Xi, H.W. Zhang, W.H. Wang, G.H. Wu, Realization of multifunctional shape-memory ferromagnets in all-d-metal Heusler phases, Appl. Phys. Lett. 107 (2015) 022406.

[18] Z.Y. Wei, E.K. Liu, Y. Li, X.L. Han, Z.W. Du, H.Z. Luo, G.D. Liu, X.K. Xi, H.W. Zhang, W.H. Wang, G.H. Wu, Magnetostructural martensitic transformations with large volume changes and magneto-strains in all-d-metal Heusler alloys, Appl. Phys. Lett. 109 (2016) 071904.

[19] H.N. Bez, A.K. Pathak, A. Biswas, N. Zarkevich, V. Balema, Y. Mudryk, D.D. Johnson, V.K. Pecharsky, Giant enhancement of the magnetocaloric response in Ni-Co-Mn-Ti by rapid solidification, Acta Mater. 173 (2019) 225–230.

[20] K. Liu, S.C. Ma, C.C. Ma, X.Q. Han, K. Yu, S. Yang, Z.S. Zhang, Y. Song, X.H. Luo, C.C. Chen, S.U. Rehman, Z.C. Zhong, Martensitic transformation and giant magneto-functional properties in all-d-metal Ni-Co-Mn-Ti alloy ribbons, J. Alloy. Compd. 790 (2019) 78–92.

[21] Y.X. Zhang, H. Zeng, G. Yu, K. Liu, S.C. Ma, K. Yang, X.W. Zhao, G. Yuan, X.H. Luo, C.C. Chen, Z.C. Zhong, Impact of annealing on the martensitic transformation and magnetocaloric properties in all-3d-metal $Mn_{50}Ni_{32}Co_8Ti_{10}$ alloy ribbons, Intermetallics 125 (2020) 106882.

[22] Z.Y. Wei, Design magnetic phase transition in MM'X -alloys and all-d-metal Heusler alloys, Nat. Commun. (2017).

[23] A. Taubel, B. Beckmann, L. Pfeuffer, N. Fortunato, F. Scheibel, S. Ener, T. Gottschall, K.P. Skokov, H.R. Zhang, O. Gutfleisch, Tailoring magnetocaloric effect in all-d-metal Ni-Co-Mn-Ti Heusler alloys: a combined experimental and theoretical study, Acta Mater. 201 (2020) 425–434.

[24] H.M. Rietveld, A profile refinement method for nuclear and magnetic structures, J. Appl. Crystallogr 2 (1969) 65–71.

[25] G. Porcari, M. Buzzi, F. Cugini, R. Pellicelli, C. Pernechele, L. Caron, E. Brück, M. Solzi, Direct magnetocaloric characterization and simulation of thermo-magnetic cycles, Rev. Sci. Instrum. 84 (2013) 073907.

[26] G. Kresse, J. Hafner, Ab initio molecular dynamics for liquid metals, Phys. Rev. B 47 (1993) 558–561.

[27] G. Kresse, J. Furthmuller, Efficiency of ab-initio total energy calculations for metals and semiconductors using a plane-wave basis set, Comp. Mater. Sci. 6 (1996) 15–50.

[28] P.E. Blochl, Projector augmented-wave method, Phys. Rev. B 50 (1994) 17953–17979.

[29] G. Kresse, D. Joubert, From ultrasoft pseudopotentials to the projector augmented-wave method, Phys. Rev. B 59 (1999) 1758–1775.

[30] J.P. Perdew, K. Burke, M. Ernzerhof, Generalized gradient approximation made simple, Phys. Rev. Lett. 78 (1997) 1396-1396.

[31] M. Methfessel, A.T. Paxton, High-precision sampling for brillouin-zone integration in metals, Phys. Rev. B 40 (1989) 3616–3621.

[32] B. Cordero, V. Gomez, A.E. Platero-Prats, M. Reves, J. Echeverria, E. Cremades, F. Barragan, S. Alvarez, Covalent radii revisited, Dalton Trans. 21 (2008) 2832–2838.

[33] S.L. Liu, H.C. Xuan, T. Cao, L.B. Wang, Z.G. Xie, X.H. Liang, H. Li, L. Feng, F.H. Chen, P.D. Han, Magnetocaloric and elastocaloric effects in all-d-metal $Ni_{37}Co_9Fe_4Mn_{35}Ti_{15}$ magnetic shape memory alloy, Phys. Status Solidi A 216 (2019) 1–7.

[34] Y. Li, S.Y. Huang, W.H. Wang, E.K. Liu, L.W. Li, Ferromagnetic martensitic transformation and large magnetocaloric effect in $Ni_{35}Co_{15-x}Fe_xMn_{35}Ti_{15}$ (x=2, 4, 6, 8) alloys, J. Appl. Phys. 127 (2020) 233907.

[35] L. Pal, K.G. Suresh, A.K. Nigam, Effect of Mn substitution on the magnetic and magneto-transport properties of $Fe_{3-x}Mn_xSi$ (0 < = x < = 1.25) alloys, J. Appl. Phys. 113 (2013) 093904.

[36] A.F. Manchon-Gordon, R. Lopez-Martin, A. Vidal-Crespo, J.J. Ipus, J.S. Blazquez, C.F. Conde, A. Conde, Distribution of transition temperatures in magnetic transformations: sources, effects and procedures to extract information from experimental data, Met. Basel 10 (2020) 1–23.

[37] G. Cavazzini, F. Cugini, D. Delmonte, G. Trevisi, L. Nasi, S. Ener, D. Koch, L. Righi, M. Solzi, O. Gutfleisch, F. Albertini, Multifunctional Ni-Mn-Ga and Ni-Mn-Cu-Ga Heusler particles towards the nanoscale by ball-milling technique, J. Alloy. Compd. 872 (2021) 159747.

[38] P. Devi, C.S. Mejia, L. Caron, S. Singh, M. Nicklas, C. Felser, Effect of chemical and hydrostatic pressure on the coupled magnetostructural transition of Ni-Mn-In Heusler alloys, Phys. Rev. Mater. 3 (2019) 122401.

[39] L. Caron, N.T. Trung, E. Brück, Pressure-tuned magnetocaloric effect in $Mn_{0.93}Cr_{0.07}CoGe$, Phys. Rev. B 84 (2011) 020414.

[40] N.T. Trung, V. Biharie, L. Zhang, L. Caron, K.H.J. Buschow, E. Brück, From single- to double-first-order magnetic phase transition in magnetocaloric $Mn_{1-x}Cr_xCoGe$ compounds, Appl. Phys. Lett. 96 (2010) 162507.

[41] P. Devi, C.S. Mejia, L. Caron, S. Singh, M. Nicklas, C. Felser, Effect of chemical and hydrostatic pressure on the coupled magnetostructural transition of Ni-Mn-In Heusler alloys, Phys. Rev. Mater. 3 (2019) 1–7.

[42] Z.B. Li, J.J. Yang, D. Li, Z.Z. Li, B. Yang, H.L. Yan, C.F. Sanchez-Valdes, J.L.S. Llamazares, Y.D. Zhang, C. Esling, X. Zhao, L. Zuo, Tuning the reversible magnetocaloric effect in Ni-Mn-In-based alloys through Co and Cu Co-doping, Adv. Electron. Mater. 5 (2019) 1800845.

[43] D.W. Zhao, J. Liu, X. Chen, W. Sun, Y. Li, M.X. Zhang, Y.Y. Shao, H. Zhang, A.R. Yan, Giant caloric effect of low-hysteresis metamagnetic shape memory alloys with exceptional cyclic functionality, Acta Mater. 133 (2017) 217–223.

[44] T. Kanomata, Y. Kitsunai, K. Sano, Y. Furutani, H. Nishihara, R.Y. Umetsu, R. Kainuma, Y. Miura, M. Shirai, Magnetic properties of quaternary Heusler alloys $Ni_{2-x}Co_xMnGa$, Phys. Rev. B 80 (2009) 214402.

[45] L.M. Wang, Z.B. Li, J.J. Yang, B. Yang, X. Zhao, L. Zuo, Large refrigeration capacity in a $Ni_{48}Co_1Mn_{37}In_{14}$ polycrystalline alloy with low thermal hysteresis, Intermetallics 125 (2020) 1–6.

[46] D.Y. Cong, S. Roth, L. Schultz, Magnetic properties and structural transformations in Ni-Co-Mn-Sn multifunctional alloys, Acta Mater. 60 (2012) 5335–5351.

[47] C. Salazar-Mejia, V. Kumar, C. Felser, Y. Skourski, J. Wosnitza, A.K. Nayak, Measurement-protocol dependence of the magnetocaloric effect in Ni-Co-Mn-Sb Heusler alloys, Phys. Rev. Appl. 11 (2019) 054006.

[48] S. Ghosh, A. Ghosh, K. Mandal, Reversible magnetocaloric effect and critical exponent analysis in Mn-Fe-Ni-Sn Heusler alloys, J. Alloy. Compd. 746 (2018) 200–205.

[49] P. Nehla, V.K. Anand, B. Klemke, B. Lake, R.S. Dhaka, Magnetocaloric properties and critical behavior of $Co_2Cr_{1-x}Mn_xAl$ Heusler alloys, J. Appl. Phys. 126 (20) (2019) 203903.

[50] E. Brück, H. Yibole, L. Zhang, A universal metric for ferroic energy materials, Philos. Trans. R. Soc. A 374 (2016) 1–6.

[51] S.-H. Whang, Nanostructured Metals and Alloys: Processing, Microstructure, Mechanical Properties and Applications, Elsevier, 2011.